JACS
JOURNAL OF THE AMERICAN CHEMICAL SOCIETY

Article

pubs.acs.org/JACS

Electrochemical Activation of CO_2 through Atomic Ordering Transformations of AuCu Nanoparticles

Dohyung Kim,[†,∇,⊗] Chenlu Xie,[§,⊗] Nigel Becknell,[§] Yi Yu,[§] Mohammadreza Karamad,[⊥,∥] Karen Chan,[⊥,∥] Ethan J. Crumlin,[#] Jens K. Nørskov,[⊥,∥] and Peidong Yang*[,†,§,‡,∇]

[†]Department of Materials Science and Engineering, University of California, Berkeley, California 94720, United States
[§]Department of Chemistry, University of California, Berkeley, California 94720, United States
[⊥]Department of Chemical Engineering, Stanford University, Stanford, California 94305, United States
[∥]SLAC National Accelerator Laboratory, Menlo Park, California 94025, United States
[#]Advanced Light Source, Lawrence Berkeley National Laboratory, Berkeley, California 94720, United States
[‡]Chemical Sciences Division, Lawrence Berkeley National Laboratory, Berkeley, California 94720, United States
[∇]Kavli Energy Nanosciences Institute, Berkeley, California 94720, United States

Supporting Information

ABSTRACT: Precise control of elemental configurations within multimetallic nanoparticles (NPs) could enable access to functional nanomaterials with significant performance benefits. This can be achieved down to the atomic level by the disorder-to-order transformation of individual NPs. Here, by systematically controlling the ordering degree, we show that the atomic ordering transformation, applied to AuCu NPs, activates them to perform as selective electrocatalysts for CO_2 reduction. In contrast to the disordered alloy NP, which is catalytically active for hydrogen evolution, ordered AuCu NPs selectively converted CO_2 to CO at faradaic efficiency reaching 80%. CO formation could be achieved with a reduction in overpotential of ∼200 mV, and catalytic turnover was enhanced by 3.2-fold. In comparison to those obtained with a pure gold catalyst, mass activities could be improved as well. Atomic-level structural investigations revealed three atomic gold layers over the intermetallic core to be sufficient for enhanced catalytic behavior, which is further supported by DFT analysis.

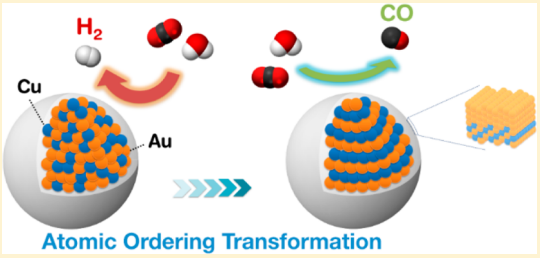

INTRODUCTION

Multimetallic nanoparticles (NPs) have great tunability in their structure and properties because of their widely tunable compositions. In this regard, they have been extensively studied for various applications, where their properties overcome the drawbacks of single-component systems.[1−3] Beyond simply controlling the ratio between the elements where each is randomly distributed, precise positioning of atoms in a crystal lattice becomes possible when there exists a thermodynamically accessible phase. This results in a distinction between a disordered alloy and an ordered intermetallic structure, and the transition between the two different phases is the so-called order−disorder transformation.[4]

Recent works on ordered intermetallic NPs have focused on developing synthetic strategies to promote ordering transformations from the initial alloy and investigating their structure and properties for applications in magnetism and catalysis.[5−12] Structurally ordered Pt-based (with Fe, Co, Cu, etc.) NPs have been under investigation in the past few years, as the ordered structure has been known to offer enhanced activity and durability for the oxygen reduction reaction (ORR).[6−9,12] On the other hand, for the other well-known bimetallic system of Au−Cu, discovery and use of its enhanced properties, attributable to its having an ordered lattice, have not been well studied, with only a few reports present regarding the synthetic approach to create ordered NPs.[5,10,11,13,14] Recently, it has been shown that Au−Cu bimetallic systems exhibit interesting electrocatalytic properties for CO_2 reduction controlled by their composition.[15,16] In this work, we investigate the effects of order−disorder transformation in AuCu NPs on electrochemical CO_2 reduction. We show that the ordering transformation of a disordered AuCu (1:1 atomic ratio) NP turns an inactive catalyst, which mainly generates hydrogen gas, to an active catalyst for reducing CO_2. This was found through systematic control of the ordering degree of AuCu NPs and observation of its effect on the catalytic behavior. We perform detailed structural investigations of ordered AuCu NPs down to the atomic level to find ordered lattice configurations, together with a few-atoms-thick Au layer on the outer surface. Furthermore, thermochemical DFT calculations suggest that the enhanced CO_2 reduction activities observed for ordered intermetallic AuCu NPs arise from the formation of compressively strained Au overlayers.

Received: April 7, 2017
Published: May 29, 2017

DOI: 10.1021/jacs.7b03516
J. Am. Chem. Soc. 2017, 139, 8329−8336

EXPERIMENTAL SECTION

Materials. Copper(II) acetate monohydrate (98%), oleic acid (90%), tri-*n*-octylamine (TOA, 98%), oleylamine (70%), borane *tert*-butylamine complex (TBAB, 97%), gold(III) chloride trihydrate ($HAuCl_4 \cdot 3H_2O$, 49% Au basis), and *o*-xylene were purchased from Sigma-Aldrich. Potassium carbonate (99.997%) was purchased from Alfa Aesar. All chemicals were used as received without further purification. Carbon dioxide (5.0 UHP) and argon (5.0 UHP) gas were purchased from Praxair.

Synthesis of Au Seed Nanoparticles. Au NPs that act as seeds during elemental copper incorporation were prepared using modified procedures from earlier work.[5] $HAuCl_4 \cdot 3H_2O$ (0.1 g) was dissolved in 10 mL of *o*-xylene and 10 mL of oleylamine at 10 °C under Ar flow and vigorous magnetic stirring. TBAB (0.5 mmol) dissolved in *o*-xylene (1 mL) and oleylamine (1 mL) via sonication was injected into the $HAuCl_4$ solution. The mixed solution was then stirred for 1 h at 10 °C before ethanol was added to precipitate Au NPs via centrifugation. The precipitate was redispersed in hexane, followed by addition of ethanol and centrifugation. The final product was dispersed in hexane for AuCu bimetallic NP synthesis.

Synthesis of AuCu Bimetallic Nanoparticles. The as-synthesized Au NPs (0.25 mmol) were dispersed in 20 mL of hexane and used as seeds for AuCu NP synthesis. A typical synthesis procedure was carried out in a Schlenk line. For the synthesis of *d*-AuCu (disordered), *i1*-AuCu, and *i2*-AuCu NPs (*i1* and *i2* at intermediate ordering), $Cu(CH_3COO)_2 \cdot H_2O$ (0.25 mmol) was mixed with oleic acid (0.25 mL) and TOA (1.125 mL) in a 25 mL three-neck flask and heated at 80 °C for 30 min to form a clear solution. Au NPs in hexane was added to this solution. Once hexane completely evaporated, the mixture was heated at 120 °C for 20 min under Ar and then quickly heated to 200 or 280 °C, and kept for 50−100 min (i.e., 200 °C 50 min, 200 °C 100 min, 280 °C 100 min for the synthesis of *d*-AuCu, *i1*-AuCu and *i2*-AuCu NPs, respectively) before it was cooled to room temperature. The product was collected by ethanol addition, centrifuged, and redispersed in 20 mL of hexane. Particularly, for the synthesis of ordered AuCu NPs (*o*-AuCu NPs), $Cu(CH_3COO)_2 \cdot H_2O$ (0.25 mmol) was dissolved in oleic acid (0.5 mL), TOA (2.25 mL), and oleylamine (0.3 mL) at 80 °C. After the addition of Au NPs/hexane solution and the evaporation of hexane, the solution was heated at 120 °C for 20 min and then quickly heated to 300 °C for 50 min. NP separation and purification steps similar to those used for the other NPs were followed.

Characterization of AuCu NPs. Powder X-ray diffraction (XRD) patterns of the AuCu NPs were obtained using a Bruker AXS D8 Advance diffractometer with a Co Kα source ($\lambda_{\text{Co K}\alpha}$ = 1.79 Å). The morphology of AuCu NPs was probed using transmission electron microscopy (TEM) on a Hitachi H-7650 and a FEI Tecnai F20 instrument. The energy-dispersive X-ray spectroscopy (EDS) elemental mapping images were recorded using an FEI Titan microscope. This instrument was equipped with an FEI Super-X Quad windowless detector that is based on silicon drift technology. Gold and copper quantitative analysis by inductively coupled plasma atomic emission spectroscopy (ICP-AES) was carried out on a PerkinElmer optical emission spectrometer (Optima 7000 DV). Before the ICP-AES measurement, the catalyst was digested in aqua regia for 24 h, and then deionized water was added to dilute the solution to a suitable concentration. X-ray photoelectron spectroscopy (XPS, PHI 5400) measurements were carried out using an Al Kα source, with the pressure inside the chamber maintained below ~4×10^{-9} Torr. The spectra were collected at a pass energy of 17.9 eV. All the spectra collected were corrected using a Shirley background. Compositions were determined by considering the atomic sensitivity factors. Ultraviolet−visible (UV−vis) absorption spectra (Vernier) were measured with NPs dispersed in solution. Aberration-corrected high-angle annular dark field (HAADF) scanning transmission electron microscopy (STEM) was performed on a double aberration-corrected TEAM0.5 microscope at 300 kV using a high-angle annular detector, resulting in "Z-contrast" images. Experimental STEM images shown in this work were deconvoluted using the maximum entropy method.[17]

Electrochemical Reduction of Carbon Dioxide. Working electrodes were prepared by drop-casting 4 μg of each AuCu NP (dispersed in hexanes) onto a carbon paper electrode (1 cm^2) and drying under vacuum at room temperature overnight. All electrochemical measurements were carried out in our customized setup, which has two compartments separated by an anion-exchange membrane (Selemion AMV). The working electrode and the counter electrode compartment hold 15 mL of electrolyte each, and the working compartment is sealed in order to allow measurements of gas products. Platinum wire was used as a counter electrode and Ag/AgCl (3 M KCl) as a reference electrode. All potentials in this work are converted to the RHE scale by $E(\text{vs RHE}) = E(\text{vs Ag/AgCl}) + 0.210\ \text{V} + 0.0591 \times \text{pH}$. The 0.1 M $KHCO_3$ electrolyte was prepared from K_2CO_3 saturated with CO_2 (pH 6.8).

During electrochemistry, CO_2 flowed through the working compartment at a rate of 30 sccm. Linear sweep voltammetry was conducted initially at a scan rate of 50 mV/s, and multiple working electrodes prepared for each sample were similar in performance. During chronoamperometry, effluent gas from the cell went through the sampling loop of a gas chromatograph (SRI) to analyze the concentration of gas products. The gas chromatograph was equipped with a molecular sieve 13X (1/8 in. × 6 ft) and hayesep D (1/8 in. × 6 ft) column with Ar flowing as a carrier gas. The separated gas products were analyzed by a thermal conductivity detector (for H_2) and a flame ionization detector (for CO). Quantification of the products was performed with the conversion factor derived from the standard calibration gases. Liquid products were analyzed afterward by qNMR (Bruker AV-500) using dimethyl sulfoxide as an internal standard. Solvent presaturation technique was implemented to suppress the water peak. Faradaic efficiencies were calculated from the amount of charge passed to produce each product, divided by the total charge passed at a specific time or during the overall run.

Computational Methods. Density Functional Theory (DFT) calculations were performed using the Quantum Espresso (QE)[18] code integrated with the Atomic Simulation Environment (ASE).[19] The revised Perdew−Burke−Ernzerhof (RPBE) functional was used for exchange and correlation,[20] which has been shown to provide better adsorption energies than the PBE functional. The ion−electron interaction was described by ultrasoft pseudo potentials.[21] The Kohn−Sham (KS) wave functions were expanded in a series of plane waves with a converged energy cutoff of 550 eV and a density cutoff of 5500 eV. The electron density was determined by the iterative diagonalization of the KS Hamiltonian using Pulay mixing of electronic densities at an electronic temperature of 0.1 eV. All total energies were extrapolated to 0 K.

The lattice parameters for the ordered $L1_0$ AuCu intermetallic within this crystal structure were calculated as a = 4.09 Å and c = 3.73 Å, in a reasonable agreement with the experimental lattice parameters of a = 3.98 Å and c = 3.72 Å in the current study and previous studies.[11]

To determine adsorption energies, the surfaces were modeled using four-layer, 3×2 slabs repeated in a supercell geometry, with at least 17 Å of vacuum between successive slabs and the bottom two layers fixed. To determine surface energies, nine-layer symmetric slabs were used with five layers fixed.[22] Slabs were relaxed until all force components were less than 0.05 eV/Å. We used a Monkhorst−Pack grid with dimensions of 4×6×1 to sample the first Brillouin zones of the surfaces.[23] In determining the adsorption energies, all sites were considered, and only the most stable ones are reported here.

To determine the thermochemical reaction energetics, we applied the computational hydrogen electrode (CHE) model,[24] which does not require explicit consideration of the solvent or solvated protons. To determine the reaction free energy ΔG of a given proton electron transfer, e.g.,

$$* + CO_2 + (H^+ + e^-) \rightarrow COOH*$$

we can determine the free energy ΔG_0 of the corresponding chemical hydrogenation reaction,

DOI: 10.1021/jacs.7b03516
J. Am. Chem. Soc. 2017, 139, 8329−8336

$$* + CO_2 + {}^1/_2H_2 \rightarrow COOH*$$

At standard pressure, the reaction $H^+ + e^- \rightleftarrows {}^1/_2H_2(g)$ is at equilibrium at 0 V_{RHE}. Therefore, $\Delta G = \Delta G_0$ at 0 V_{RHE}, and in general, $\Delta G(U) = \Delta G_0 + eU$. We also define a limiting potential U_L, the potential at which the reaction step becomes exergonic: $U_L = -\Delta G_0/e$. Since barriers scale with reaction energies,[25] trends in U_L should follow trends in activity. In the case of CO_2 reduction toward methane and methanol, this potential has been shown previously to correlate well with experimental activities on transition metals.[26,27] We have applied a simple −0.25 eV correction to *COOH adsorption energies to account for solvation, as was determined in previous works.[27]

RESULTS AND DISCUSSION

AuCu bimetallic nanoparticles with varying degrees of atomic ordering were realized by synthetic procedures modified from earlier work.[5] Mainly, temperature and time were controlled during the incorporation of elemental copper into the gold NP seed (Figure S1), where higher temperatures and longer times promote the formation of ordered lattices. Since we start from identical seed particles, AuCu bimetallic NPs with similar sizes (~7 nm) could be produced that look identical in their morphologies (Figure 1 and Figure S2). Au-to-Cu ratios, identified from ICP-AES (Figure S3), are all around 1, confirming their compositional invariance.

The structural difference between AuCu NPs could be identified from XRD. As shown in Figure 1b, the peak positions of 111 and 200 diffractions further confirmed the formation of a bimetallic system, as they lie between those of pure Au and Cu. However, there was a trend where the superlattice peaks, which should be absent in a disordered face-centered cubic (FCC) structure of an alloy, became more evident in the NPs synthesized at higher temperatures for extended periods. Moreover, peak splitting became clearer as well at the 200 and 220 positions, indicating that the crystal structure was transitioning from FCC to face-centered tetragonal. All of these indicated an increase in the degree of atomic ordering following greater input of energy (controlled with temperature and time) during Cu diffusion into Au NP.[5,10,11]

The degree of ordering was further quantified by the long-range order parameter (S), estimated from the relative intensity ratio between the superlattice peak and the fundamental peak (see Supporting Information for details).[28] The AuCu NP synthesized at 300 °C had the highest S value of 0.611, which corresponded to ~80% of atoms in the ordered lattice positions. After the second most ordered AuCu NP (synthesized at 280 °C 100 min), the degree of ordering could not be quantified by S for the other two NPs, which had only short-range order. Combining the qualitative and quantitative comparisons of degree of ordering among the four AuCu NPs, we could conclude that the AuCu NP synthesized at 200 °C for 50 min (hereafter *d*-AuCu) was disordered (or the least ordered) and the one synthesized at 300 °C for 50 min (hereafter *o*-AuCu) was ordered (or the most ordered). The AuCu NPs at intermediate stages of ordering were named as *i1*-AuCu and *i2*-AuCu.

To study their activity toward electrochemical reduction of CO_2, identical numbers of each type of AuCu NP (mass of 4 μg total) were loaded on carbon paper electrodes (Figure S4). Each NP sample was washed multiple times to the point just before the NP solution became unstable, and the mass fraction of ligands in each sample was kept similar (Figure S5). Any thermal or chemical treatments were avoided so as not to alter their inherent structure produced. Each electrode was then

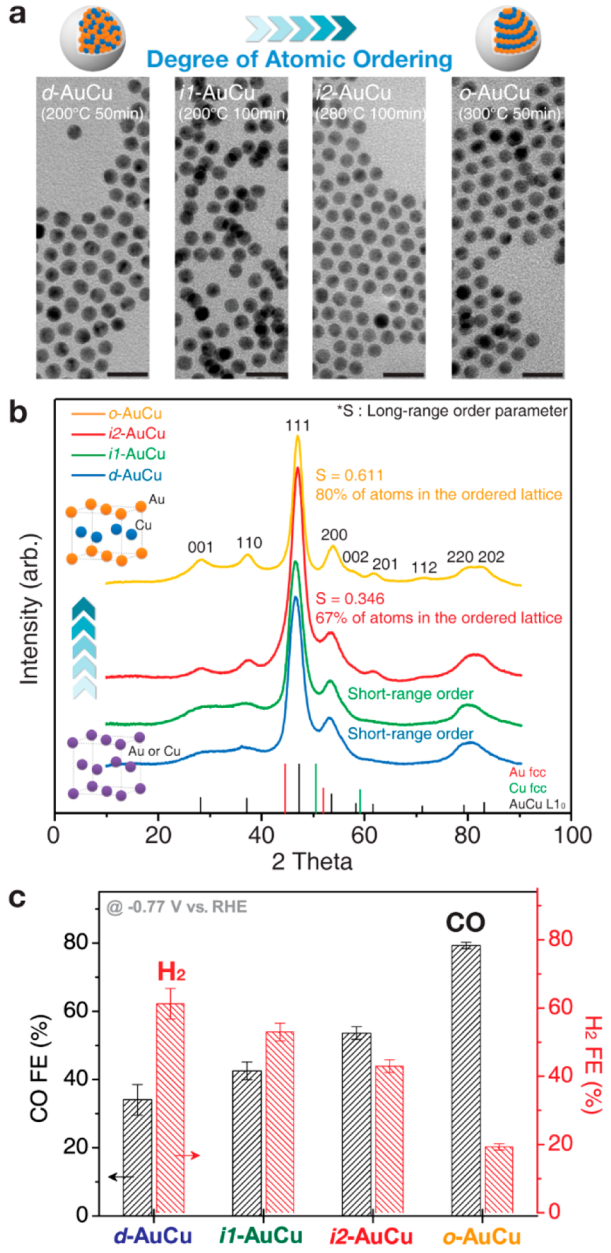

Figure 1. Atomic ordering transformation of AuCu bimetallic nanoparticles. (a) TEM images of AuCu bimetallic NPs synthesized at various conditions allowing for systematic tuning of the degree of ordering. Scale bar, 20 nm. (b) XRD of AuCu bimetallic NPs. Diffractograms were recorded using Co Kα radiation ($\lambda_{Co\ K\alpha}$ = 1.79 Å). (c) Electrochemical CO_2 reduction activities of AuCu bimetallic NPs evaluated by faradaic efficiencies of CO and H_2. Measurements were conducted at −0.77 V vs RHE with 0.1 M $KHCO_3$ solution (pH 6.8) at 1 atm CO_2 and room temperature.

tested in a customized electrochemical setup under conditions of 0.1 M $KHCO_3$ (pH 6.8) at 1 atm CO_2 and room temperature. Linear sweep voltammetry of AuCu NPs resulted in similar current densities from utilizing same number of NPs with identical morphology for each and providing equal surface area (Figure S6). During chronoamperometry, gas products were measured *in situ* using gas chromatography, and liquid products were analyzed from quantitative nuclear magnetic resonance (qNMR) spectroscopy.

DOI: 10.1021/jacs.7b03516
J. Am. Chem. Soc. 2017, 139, 8329−8336

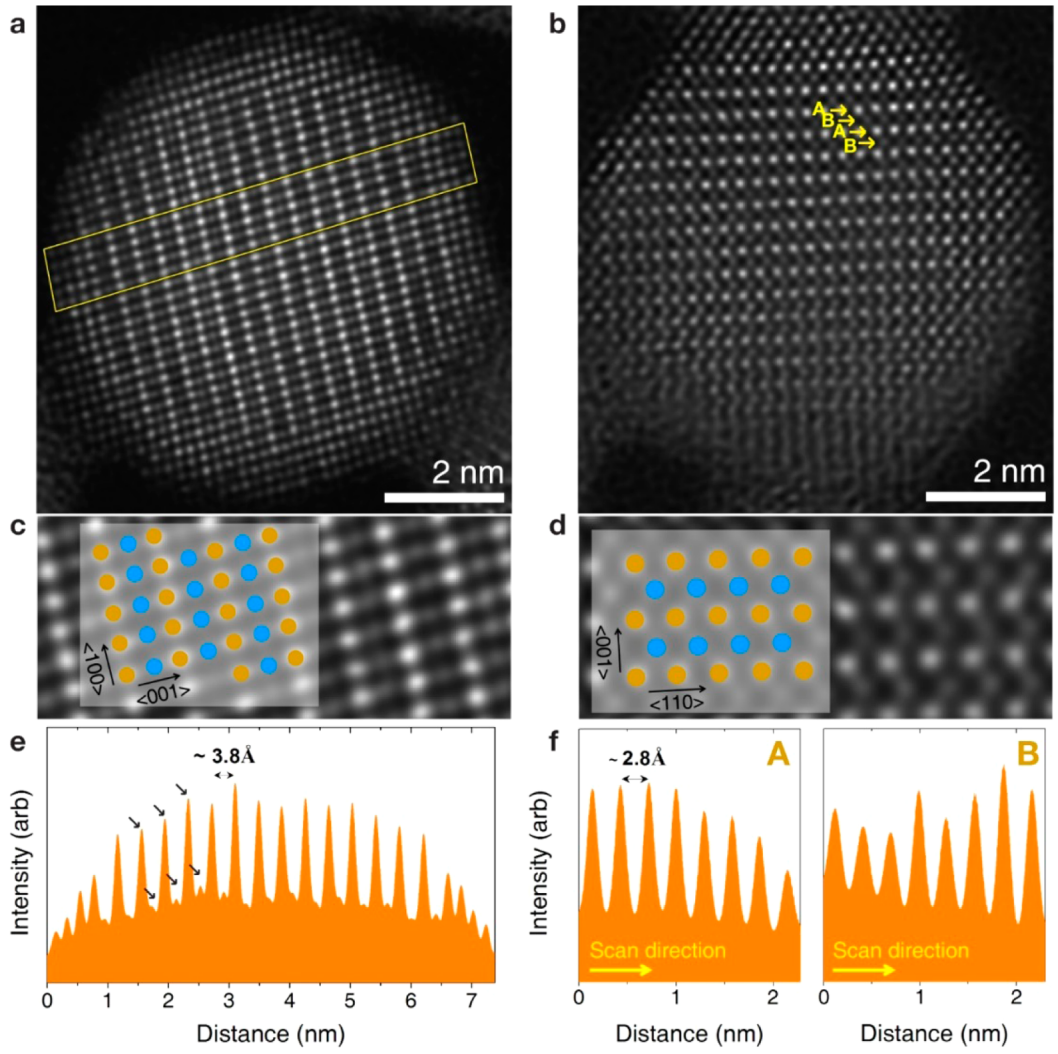

Figure 2. Structural investigation of *o*-AuCu at atomic resolution. Aberration-corrected HAADF-STEM images of *o*-AuCu (a,b) and magnified STEM images of the center of the particle together with the overlapping schematics of structure projections (c,d). Atoms in orange and blue color represent gold and copper, respectively. (e) Intensity profile across the particle measured from the yellow box shown in (a). The distance between the strong intensities matches with the separation between gold atoms. Arrows indicate alternating high and low intensities, which represent gold and copper atoms, respectively. (f) Average intensity profile from the interior to the outer surface of the particle along rows A and B shown in (b). The distance between the peaks shown in A matches with the known separation between gold atoms.

The major products formed were CO and H_2, and their faradaic efficiencies (FE) were measured at −0.77 V vs RHE (Figure 1c). The only liquid product found was formate at relatively low FE < 5% (Figure S7). For the *d*-AuCu NP, H_2 was the dominant product (H_2 FE ≈ 61% and CO FE ≈ 34%), which meant it was considered rather inactive for electrochemical CO_2 reduction. However, a continuous rise was observed in CO FE with increase in the ordering degree of AuCu NPs, where *o*-AuCu NP exhibited the highest CO selectivity. CO became the major product for *o*-AuCu NP, with FE ≈ 80%. Previous study on the effects of composition in Au−Cu alloys for electrocatalytic CO_2 reduction has shown that H_2 is the major product for AuCu (1:1 ratio), consistent with what we observe from *d*-AuCu or *i1*-AuCu.[15] Surprisingly, without altering composition, we found that the ordering transformation could enhance CO formation, transitioning a CO_2 inactive catalyst to an active catalyst with high CO selectivity. The CO FEs measured at a range of potentials for *d*-AuCu and *o*-AuCu NP further confirmed the activity enhancement following disorder-to-order transformation, where CO formation could be obtained at ∼200 mV lower overpotentials (Figure S8).

In order to understand this drastic change in activity that arises from the ordering transformation of a AuCu bimetallic NP, we probed the structure of *d*-AuCu and *o*-AuCu NP using various methods. Elemental analysis mapping of the distribution of Au and Cu showed that both elements were uniformly distributed in a single NP for both *d*-AuCu and *o*-AuCu NP (Figure S9). In order to investigate down to the atomic level, aberration-corrected HAADF-STEM was implemented. Figure 2a,b show aberration-corrected HAADF-STEM images of *o*-AuCu NPs in two different orientations. From the images, a periodic oscillation of intensity was observed, which can be attributed to the *Z*-contrast differences between different elements that should be present in an ordered lattice. As Au (Z = 79) and Cu (Z = 29) differ greatly in atomic number, a column of Au atoms should appear much brighter than that of Cu atoms in an ordered structure. By measuring the distance between the planes and distinguishing elements by their

DOI: 10.1021/jacs.7b03516
J. Am. Chem. Soc. 2017, 139, 8329−8336

contrast, certain unit cell orientations of the AuCu $L1_0$ structure were found (Figure 2c,d).

In addition to the atomically ordered structures that were verified, certain elemental characteristics at the surface were also observed. As can be directly seen from the images, atoms near the NP surface contained only brighter intensities of gold, in contrast to the alternating intensities at the core. This suggested a few-atoms-thick gold layer over the structurally ordered core. With the intensity profile measured across the particle (Figure 2e), a three-atoms-thick gold layer could be identified. Intensities were also measured along the rows of atoms which should contain only one element (Figure 2f). While the intensity along the row of gold atoms decayed to the surface (from the thickness decreasing), the intensity profile along what is supposed to be only copper atoms had spiking intensities starting from three atoms beneath the surface. All of these pointed to the fact that *o*-AuCu NP contained around three-atoms-thick gold layers grown directly over the ordered lattice. This could be observed in multiple images as well (Figure S10). In contrast, aberration-corrected HAADF-STEM images of *d*-AuCu NPs exhibited uniform intensities (Figure S11) from the random distribution of both elements, as expected. From atomically resolved imaging of *o*-AuCu NPs, we could conclude that the ordering transformation of a AuCu NP induced three-atoms-thick gold layers at its surface, in addition to the crystal structure transition to intermetallic ordered phase throughout its interior.

XAS was used to further probe the structure of AuCu NPs. Absorption spectra at the gold L_3-edge and copper K-edge were collected from *o*-AuCu NPs and *d*-AuCu NPs (Figure S12). Figure 3 presents extended X-ray absorption fine structure (EXAFS) data for both NPs, where the coordination environment surrounding Au and Cu for each NP can be observed. At the Au L_3-edge (Figure 3a), *o*-AuCu NP exhibits a larger first-shell scattering amplitude, which can be attributed to the stronger constructive interference of photoelectron scattering in the ordered structure. The atomic order is more evident at the Cu K-edge (Figure 3b), where third and fourth shell scattering (at radial distances from 4 to 6 Å) can be clearly observed due to the unique multiple scattering paths present in the ordered structure. On the other hand, *d*-AuCu NP at the Cu K-edge shows many variations of scattering paths at various lengths, together with destructive interference from the disordered structure, which lowers the amplitude.

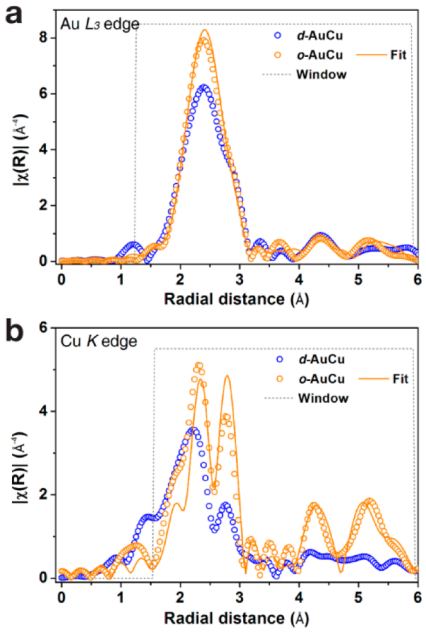

Figure 3. X-ray absorption spectroscopy of AuCu NPs. EXAFS spectra at the Au L_3-edge (a) and Cu K-edge (b) of *o*-AuCu NPs (orange circles) and *d*-AuCu NPs (blue circles). Orange solid lines are the results of fitting to *o*-AuCu NPs.

By fitting the Au L_3-edge and Cu K-edge of the *o*-AuCu NPs simultaneously to an ordered face-centered tetragonal ($L1_0$) model, information regarding the coordination environment surrounding gold and copper atoms in *o*-AuCu NPs could be extracted (Tables S1 and S2). When comparing the number of nearest neighbor atoms to gold and copper, copper had a coordination number (CN) of 9.0 ± 1.2, while gold had a CN of only 6.9 ± 1.1. The lower first shell CN for gold indicated that gold atoms are relatively undercoordinated compared to copper, which resulted from gold being enriched at the surface[29] as observed from HAADF-STEM. Therefore, from STEM imaging and XAS analysis, we could conclude that the *o*-AuCu NP surface contains a three-atoms-thick gold layer over the ordered AuCu intermetallic core. Furthermore, we speculate NPs at intermediate stages of ordering to have gold overlayers partially covering their surface. Rise in the degree of ordering may lead to increased coverage of gold overlayers associated with the ordered phase (Figure S13). XPS (Figure S14) and UV−vis spectroscopy (Figure S15) were used to further prove that the gold overlayer is only a few atoms thick and not significant enough to be detected by these techniques.[30]

From the structural investigation of *o*-AuCu NPs, we found the formation of a three-atoms-thick gold overlayer following ordering transformation. This suggests that surface enrichment of gold at atomic levels may be the origin of enhanced catalytic behavior. Identifying the precise structures of surface active sites is necessary to gain catalytic insights. Here, we have identified the catalytically active surface structure of a ordered AuCu NP and this may well be extended to other ordered bimetallic systems involving noble and non-noble element mixtures, such as the Cu−Pd system recently demonstrated for CO_2 reduction.[31]

To further investigate electrocatalytic activities for reducing carbon dioxide, CO production rates measured in terms of specific current density (mA/cm^2) and mass activity (A/g_{Au}) were probed for AuCu bimetallic NPs, in addition to the FE (Figure 4). Catalytic activity of pure Au NPs (Figure S16) of same size was compared as well to assess the effects of having a few-atoms-thick Au layer directly over the ordered core. Beyond having NPs of the same dimension with identical numbers to match active surface areas, surface areas were estimated using electrochemical methods. With *o*-AuCu NPs having a three-atoms-thick gold layer on the surface, underpotential deposition of copper in acidic media could be stably performed to estimate their surface area (Figure S17).[32,33] The same procedure was conducted on Au NPs as well and yielded comparable surface areas.

Figure 4a shows CO FEs at −0.77 V vs RHE, where atomic ordering drastically converts AuCu NPs to be selective for CO production as mentioned above. Indeed, this trend is accompanied by rise in the specific CO current density from 0.43 mA/cm^2 for *d*-AuCu NP to 1.39 mA/cm^2 for *o*-AuCu NP (Figure 4b). Therefore, we find that atomic ordering in a AuCu

DOI: 10.1021/jacs.7b03516
J. Am. Chem. Soc. 2017, 139, 8329−8336

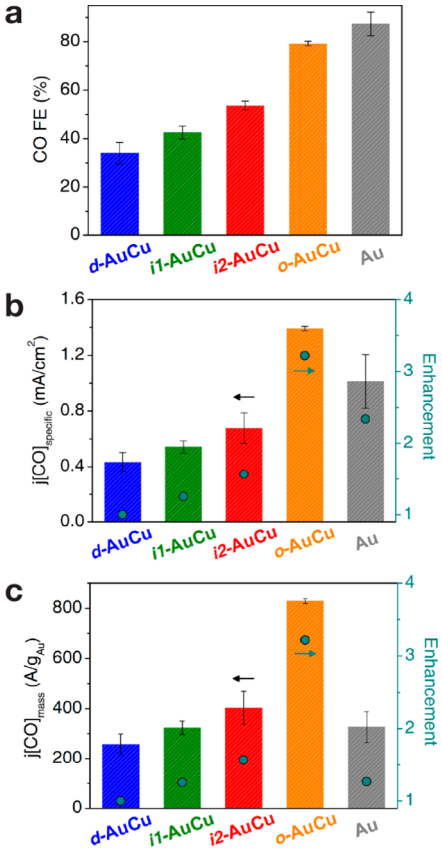

Figure 4. Electrocatalytic CO_2 reduction activity of AuCu NPs: CO faradaic efficiencies (a), CO partial current densities (b), and CO mass activities (c) of *d*-AuCu NP, *i1*-AuCu NP, *i2*-AuCu NP, *o*-AuCu NP, and Au NP for electrochemical reduction of CO_2 at −0.77 V vs RHE. CO partial current densities are specific current densities based on actual surface area of NP catalysts measured by Cu underpotential deposition on *o*-AuCu NP and Au NP. Electrochemically active surface areas of *d*-AuCu NP, *i1*-AuCu NP and *i2*-AuCu NP were estimated from the value measured of *o*-AuCu NP. CO mass activities are based on the actual mass of gold (g_{Au}) loaded for each catalyst. Green circles in (b) and (c) indicate enhancements over the activity of *d*-AuCu NP, which is set to 1.

bimetallic NP enhanced the intrinsic activity for CO_2-to-CO conversion by 3.2-fold (Figure S18), suggesting the importance of precise control of atomic arrangements in bimetallic NPs for catalytic purposes.

Interestingly, when *o*-AuCu NPs were compared to Au NPs, Au NPs exhibited higher CO selectivity, while *o*-AuCu NPs showed higher activity. Au NPs had a CO FE of 87% and a specific current density of 1.01 mA/cm^2. A similar trend in CO FE and specific current density was observed at other potentials as well (Figure S19). This indicated that a three-atoms-thick gold layer over the intermetallic core possesses different catalytic properties, such as the intermediate binding strength, to a pure gold lattice.

Here, we also probed mass activities (A/g_{Au}) for CO formation and, as shown in Figure 4c, AuCu NPs are clearly advantageous for CO production with even NPs at intermediate ordering, such as *i1*-AuCu NP, reaching comparable activities to Au NP at ∼320 A/g_{Au}. For the *o*-AuCu NP, CO mass activity reaches up to ∼830 A/g_{Au}, which is 2.6-fold over that of Au NP. The *o*-AuCu NP catalyst was also relatively stable for extended periods of 12 h (Figure S20). However, there was still a steady loss of activity (∼15%) and this might be linked to the structural stability of gold overlayers induced in the ordered structure, as some loss of gold was observed. For electrochemically producing carbon monoxide, which is considered as the most economically viable so far among various CO_2 reduction products for downstream processing to useful chemicals,[34] various types of gold-based nanostructures have been demonstrated.[32,33,35−38] We find that creating a Au−Cu bimetallic system with induced atomic ordering could be an effective strategy for promoting efficient processing of CO_2, where the structural motifs found here can also be translated to other Au-based morphologies that provide higher current output.[38] Certainly, further efforts are needed to ensure catalytic stability of the motifs found here to the levels required for industrially relevant applications.

The origin of enhanced CO_2 reduction activity by atomic ordering transformations and the resulting three-atoms-thick gold overlayer of AuCu NPs was investigated using DFT calculations. Here, we modeled a (211) facet, since it has been shown that step sites are considerably more energetically favorable for the reactions involved than terrace sites[39] and catalytic activity should be dominated by the step sites.[36] Figure 5a shows the model systems considered for AuCu NPs. *o*-AuCu

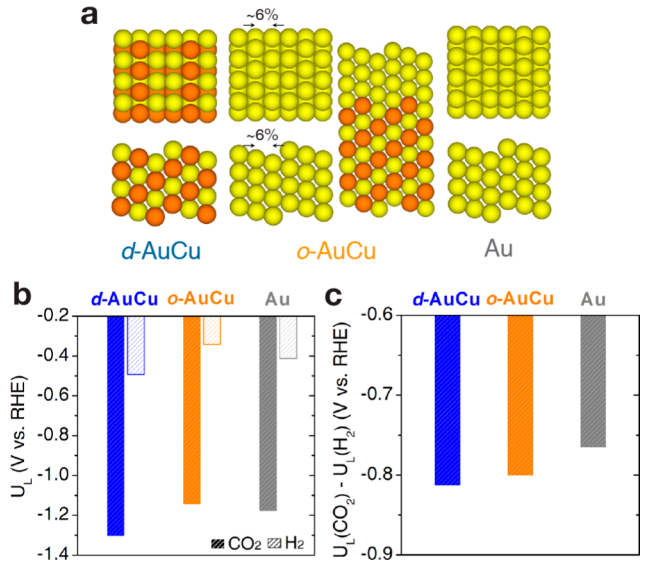

Figure 5. Computational results of CO_2 reduction on AuCu surfaces. (a) Top and side views of model 211 slabs for *d*-AuCu NP, *o*-AuCu NP, and Au NP. (b) Calculated limiting potentials for CO_2 reduction and H_2 evolution on model systems. (c) The difference in limiting potentials for CO_2 reduction and H_2 evolution on model systems.

NP was modeled as a strained Au(211) surface, since the underlying intermetallic AuCu lattice compressively strains (∼6%) the few-atoms-thick Au layer from its original lattice parameter. In principle, the underlying AuCu phase could also have an electronic effect on the Au overlayers. However, previous theoretical studies have shown that the electronic effect is essentially negligible at transition metal overlayers that are approximately three monolayers thick.[40−43] For the *d*-AuCu NPs, surface stability of various site motifs was investigated (Figure S21). Here, we assumed that the surface of *d*-AuCu NPs would be in a metastable state with mixed Au/Cu elemental configuration that has local, short-range order. Of the various (211) facets, the Au-rich (211) step had the lowest

DOI: 10.1021/jacs.7b03516
J. Am. Chem. Soc. 2017, 139, 8329−8336

surface energy. A model Au(211) surface in its original lattice configuration was also investigated as a comparison.

The reduction of CO_2 to CO occurs through a COOH intermediate bound to the active site.[44−46] For the metals that bind CO weakly, desorption of CO readily occurs, and the formation of COOH* is the potential-limiting step, where * represents a surface site. On the other hand, hydrogen evolution involves H* as the only adsorbed intermediate, and the binding energy of H* has been shown to be a reasonable descriptor of hydrogen evolution activity.[47,48]

Figure 5b compares the thermodynamic limiting potentials $U_L(CO_2)$ and $U_L(H_2)$ for the three model systems. Since activation barriers scale linearly with binding energies, trends in limiting potentials reflect trends in catalytic turnover.[25] Based on this analysis, $U_L(CO_2)$ of *o*-AuCu NP is most positive followed by Au NP and *d*-AuCu NP and therefore CO_2-to-CO conversion activity would decrease in the order of *o*-AuCu NP > Au NP > *d*-AuCu NP, which is in agreement to the trend observed experimentally. Recent DFT calculations on transition metals have suggested that the difference between the limiting potentials for CO_2 reduction and H_2 evolution (i.e., $U_L(CO_2)-U_L(H_2)$) can be linked to the trends in experimentally observed CO_2 reduction selectivity.[39] With $U_L(CO_2)$ being more negative than $U_L(H_2)$ for all transition metals, more positive $U_L(CO_2)-U_L(H_2)$ corresponds to higher selectivity toward CO_2 reduction. The trend observed for $U_L(CO_2)-U_L(H_2)$, as shown in Figure 5c, suggests that selectivity toward CO_2 reduction decreases in the order of Au NP > *o*-AuCu NP > *d*-AuCu NP, consistent with the experimental trends.

From the thermochemical DFT analysis, we find that the activity of *o*-AuCu NP originates from the compressively strained three-atoms-thick gold layers formed over the AuCu intermetallic core. We note that, while the differences in energetics appear to be only ~0.1 eV, such shifts can provide order of magnitude changes in activity, since the turnover frequencies vary exponentially with activation barriers, which scale linearly with binding energies. Furthermore, projected density of states of the model systems predict a similar trend as well (Figure S22), which shows that the ordering transformation in AuCu should favor CO_2 reduction.

CONCLUSION

The exquisite control of atomic arrangements in unit cells of bimetallic systems to an individual nanoparticle level could be a promising approach to induce interesting properties and understand their structural origin. The effect of ordering transformations in AuCu bimetallic NPs on their electrocatalytic activity for CO_2 reduction was studied, where ordered AuCu NPs selectively reduced CO_2, in contrast to disordered AuCu NPs that favored hydrogen evolution. With structure-probing techniques down to the atomic level, the enhanced activity was attributed to compressively strained three-atoms-thick gold overlayers that formed over the intermetallic core, resulting from the disorder-to-order transformation. With a large number of multimetallic systems accessible, we expect the method of regulating phase transformation between disordered alloys and ordered intermetallics in nanomaterials to have great potential in areas where control over the level of atomic precision is desired.

ASSOCIATED CONTENT

Supporting Information

The Supporting Information is available free of charge on the ACS Publications website at DOI: 10.1021/jacs.7b03516.

Experimental details and additional characterization data, including Figures S1−S22 and Tables S1 and S2 (PDF)

AUTHOR INFORMATION

Corresponding Author

*p_yang@berkeley.edu

ORCID

Dohyung Kim: 0000-0003-0201-9082
Chenlu Xie: 0000-0001-9215-6878
Karen Chan: 0000-0002-6897-1108
Ethan J. Crumlin: 0000-0003-3132-190X
Peidong Yang: 0000-0003-4799-1684

Author Contributions

⊗D.K. and C.X. contributed equally.

Notes

The authors declare no competing financial interest.

ACKNOWLEDGMENTS

This work was supported by Director, Office of Science, Office of Basic Energy Sciences, Chemical Sciences, Geosciences, & Biosciences Division, of the U.S. Department of Energy under Contract No. DE-AC02-05CH11231, FWP No. CH030201 (Catalysis Research Program). HAADF-STEM and EDS mapping made use of the instruments at the National Center for Electron Microscopy at the Molecular Foundry. XPS and SEM made use of the instruments at imaging and nanofabrication facilities at the Molecular Foundry. Work at the Molecular Foundry was supported by the Office of Science, Office of Basic Energy Sciences, of the U.S. Department of Energy under Contract No. DE-AC02-05CH11231. We acknowledge Matthew Marcus and the use of Beamline 10.3.2 at the Advanced Light Source for collection of XAS data. The Advanced Light Source is supported by the Director, Office of Science, Office of Basic Energy Sciences, of the U.S. Department of Energy under Contract No. DE-AC02-05CH11231. DFT calculations were supported by the Global Climate Energy Project (GCEP) at Stanford University (Fund No. 52454). This work made use of the facilities at the NMR facility, College of Chemistry, University of California, Berkeley. ICP-AES measurement was supported by the Microanalytical facility, College of Chemistry, University of California, Berkeley. The authors acknowledge Prof. Alivisatos for use of the X-ray diffractometer. D.K. acknowledges support from Samsung Scholarship. C.X. acknowledges support from a Suzhou Industrial Park fellowship.

REFERENCES

(1) Gilroy, K. D.; Ruditskiy, A.; Peng, H.-C.; Qin, D.; Xia, Y. *Chem. Rev.* **2016**, *116* (18), 10414.
(2) Wang, D.; Li, Y. *Adv. Mater.* **2011**, *23* (9), 1044.
(3) Sankar, M.; Dimitratos, N.; Miedziak, P. J.; Wells, P. P.; Kiely, C. J.; Hutchings, G. J. *Chem. Soc. Rev.* **2012**, *41*, 8099.
(4) Porter, D. A.; Easterling, K. E.; Sherif, M. Y. *Phase Transformations in Metals and Alloys*, 3rd ed.; CRC Press: Boca Raton, FL, 2009.
(5) Chen, W.; Yu, R.; Li, L.; Wang, A.; Peng, Q.; Li, Y. *Angew. Chem., Int. Ed.* **2010**, *49* (16), 2917.

DOI: 10.1021/jacs.7b03516
J. Am. Chem. Soc. 2017, 139, 8329−8336

(6) Jia, Q.; Caldwell, K.; Ramaker, D. E.; Ziegelbauer, J. M.; Liu, Z.; Yu, Z.; Trahan, M.; Mukerjee, S. *J. Phys. Chem. C* **2014**, *118* (35), 20496.
(7) Kim, J.; Lee, Y.; Sun, S. *J. Am. Chem. Soc.* **2010**, *132* (14), 4996.
(8) Li, Q.; Wu, L.; Wu, G.; Su, D.; Lv, H.; Zhang, S.; Zhu, W.; Casimir, A.; Zhu, H.; Mendoza-Garcia, A.; Sun, S. *Nano Lett.* **2015**, *15* (4), 2468.
(9) Prabhudev, S.; Bugnet, M.; Bock, C.; Botton, G. A. *ACS Nano* **2013**, *7* (7), 6103.
(10) Sra, A. K.; Ewers, T. D.; Schaak, R. E. *Chem. Mater.* **2005**, *17* (4), 758.
(11) Sra, A. K.; Schaak, R. E. *J. Am. Chem. Soc.* **2004**, *126* (21), 6667.
(12) Wang, D.; Xin, H. L.; Hovden, R.; Wang, H.; Yu, Y.; Muller, D. a.; DiSalvo, F. J.; Abruña, H. D. *Nat. Mater.* **2012**, *12* (1), 81.
(13) Wang, G.; Xiao, L.; Huang, B.; Ren, Z.; Tang, X.; Zhuang, L.; Lu, J. *J. Mater. Chem.* **2012**, *22* (31), 15769.
(14) Zhang, N.; Chen, X.; Lu, Y.; An, L.; Li, X.; Xia, D.; Zhang, Z.; Li, J. *Small* **2014**, *10* (13), 2662.
(15) Kim, D.; Resasco, J.; Yu, Y.; Asiri, A. M.; Yang, P. *Nat. Commun.* **2014**, *5* (May), 4948.
(16) Xu, Z.; Lai, E.; Shao-Horn, Y.; Hamad-Schifferli, K. *Chem. Commun.* **2012**, *48* (111), 5626.
(17) Grillo, V.; Rotunno, E. *Ultramicroscopy* **2013**, *125*, 97.
(18) Giannozzi, P.; Baroni, S.; Bonini, N.; Calandra, M.; Car, R.; Cavazzoni, C.; Ceresoli, D.; Chiarotti, G. L.; Cococcioni, M.; Dabo, I.; Dal Corso, A.; de Gironcoli, S.; Fabris, S.; Fratesi, G.; Gebauer, R.; Gerstmann, U.; Gougoussis, C.; Kokalj, A.; Lazzeri, M.; Martin-Samos, L.; Marzari, N.; Mauri, F.; Mazzarello, R.; Paolini, S.; Pasquarello, A.; Paulatto, L.; Sbraccia, C.; Scandolo, S.; Sclauzero, G.; Seitsonen, A. P.; Smogunov, A.; Umari, P.; Wentzcovitch, R. M. *J. Phys.: Condens. Matter* **2009**, *21*, 395502.
(19) Bahn, S. R.; Jacobsen, K. W. *Comput. Sci. Eng.* **2002**, *4* (3), 56.
(20) Hammer, B.; Hansen, L.; Nørskov, J. *Phys. Rev. B: Condens. Matter Mater. Phys.* **1999**, *59* (11), 7413.
(21) Vanderbilt, D. *Phys. Rev. B: Condens. Matter Mater. Phys.* **1990**, *41* (11), 7892.
(22) Dannenberg, A.; Gruner, M. E.; Hucht, A.; Entel, P. *Phys. Rev. B: Condens. Matter Mater. Phys.* **2009**, *80* (24), 245438.
(23) Monkhorst, H. J.; Pack, J. D. *Phys. Rev. B* **1976**, *13* (12), 5188.
(24) Nørskov, J. K.; Rossmeisl, J.; Logadottir, A.; Lindqvist, L.; Kitchin, J. R.; Bligaard, T.; Jónsson, H. *J. Phys. Chem. B* **2004**, *108* (46), 17886.
(25) Wang, S.; Petzold, V.; Tripkovic, V.; Kleis, J.; Howalt, J. G.; Skúlason, E.; Fernández, E. M.; Hvolbæk, B.; Jones, G.; Toftelund, A.; Falsig, H.; Björketun, M.; Studt, F.; Abild-Pedersen, F.; Rossmeisl, J.; Nørskov, J. K.; Bligaard, T. *Phys. Chem. Chem. Phys.* **2011**, *13* (46), 20760.
(26) Kuhl, K. P.; Hatsukade, T.; Cave, E. R.; Abram, D. N.; Kibsgaard, J.; Jaramillo, T. F. *J. Am. Chem. Soc.* **2014**, *136* (40), 14107.
(27) Peterson, A. A.; Abild-Pedersen, F.; Studt, F.; Rossmeisl, J.; Nørskov, J. K. *Energy Environ. Sci.* **2010**, *3* (9), 1311.
(28) Cullity, B. D.; Stock, S. R. *Elements of X-Ray Diffraction*, 3rd ed.; Pearson: London, 2001.
(29) Sinfelt, J. H.; Via, G. H.; Lytle, F. W. *J. Chem. Phys.* **1980**, *72* (9), 4832.
(30) Knauer, A.; Eisenhardt, A.; Krischok, S.; Koehler, J. M. *Nanoscale* **2014**, *6* (10), 5230.
(31) Ma, S.; Sadakiyo, M.; Heima, M.; Luo, R.; Haasch, R. T.; Gold, J. I.; Yamauchi, M.; Kenis, P. J. A. *J. Am. Chem. Soc.* **2017**, *139* (1), 47.
(32) Feng, X.; Jiang, K.; Fan, S.; Kanan, M. W. *J. Am. Chem. Soc.* **2015**, *137* (14), 4606.
(33) Chen, Y.; Li, C. W.; Kanan, M. W. *J. Am. Chem. Soc.* **2012**, *134* (49), 19969.
(34) Verma, S.; Kim, B.; Jhong, H. R. M.; Ma, S.; Kenis, P. J. A. *ChemSusChem* **2016**, *9*, 1972.
(35) Kauffman, D. R.; Alfonso, D.; Matranga, C.; Qian, H.; Jin, R. *J. Am. Chem. Soc.* **2012**, *134* (24), 10237.
(36) Zhu, W.; Michalsky, R.; Metin, Ö.; Lv, H.; Guo, S.; Wright, C. J.; Sun, X.; Peterson, A. A.; Sun, S. *J. Am. Chem. Soc.* **2013**, *135* (45), 16833.
(37) Zhu, W.; Zhang, Y.-J.; Zhang, H.; Lv, H.; Li, Q.; Michalsky, R.; Peterson, A. A.; Sun, S. *J. Am. Chem. Soc.* **2014**, *136* (46), 16132.
(38) Liu, M.; Pang, Y.; Zhang, B.; De Luna, P.; Voznyy, O.; Xu, J.; Zheng, X.; Dinh, C. T.; Fan, F.; Cao, C.; de Arquer, F. P. G.; Safaei, T. S.; Mepham, A.; Klinkova, A.; Kumacheva, E.; Filleter, T.; Sinton, D.; Kelley, S. O.; Sargent, E. H. *Nature* **2016**, *537* (7620), 382.
(39) Shi, C.; Hansen, H. A.; Lausche, A. C.; Nørskov, J. K. *Phys. Chem. Chem. Phys.* **2014**, *16* (10), 4720.
(40) Escudero-Escribano, M.; Verdaguer-Casadevall, A.; Malacrida, P.; Grønbjerg, U.; Knudsen, B. P.; Jepsen, A. K.; Rossmeisl, J.; Stephens, I. E. L.; Chorkendorff, I. *J. Am. Chem. Soc.* **2012**, *134* (40), 16476.
(41) Stephens, I. E. L.; Bondarenko, A. S.; Grønbjerg, U.; Rossmeisl, J.; Chorkendorff, I. *Energy Environ. Sci.* **2012**, *5* (5), 6744.
(42) Strasser, P.; Koh, S.; Anniyev, T.; Greeley, J.; More, K.; Yu, C.; Liu, Z.; Kaya, S.; Nordlund, D.; Ogasawara, H.; Toney, M. F.; Nilsson, A. *Nat. Chem.* **2010**, *2* (6), 454.
(43) Kitchin, J. R.; Nørskov, J. K.; Barteau, M. A.; Chen, J. G. *J. Chem. Phys.* **2004**, *120* (21), 10240.
(44) Hansen, H. A.; Shi, C.; Lausche, A.; Peterson, A.; Nørskov, J. K. *Phys. Chem. Chem. Phys.* **2016**, *18*, 9194.
(45) Peterson, A. A.; Nørskov, J. K. *J. Phys. Chem. Lett.* **2012**, *3* (2), 251.
(46) Hansen, H. A.; Varley, J. B.; Peterson, A. A.; Nørskov, J. K. *J. Phys. Chem. Lett.* **2013**, *4* (3), 388.
(47) Greeley, J.; Nørskov, J. K.; Kibler, L. A.; El-Aziz, A. M.; Kolb, D. M. *ChemPhysChem* **2006**, *7* (5), 1032.
(48) Greeley, J.; Jaramillo, T. F.; Bonde, J.; Chorkendorff, I. B.; Nørskov, J. K. *Nat. Mater.* **2006**, *5* (11), 909.

DOI: 10.1021/jacs.7b03516
J. Am. Chem. Soc. 2017, 139, 8329−8336